

Thermal performance of automotive radiators made of plastic and stainless steel microtubes

Ilja Astrouski^{a,*}, Krystof Mraz^a, Jan Bohacek^a, Ales Horak^b, Erik Bartuli^a

^a Heat Transfer and Fluid Flow Laboratory, Faculty of Mechanical Engineering, Brno University of Technology, Technická 2896/2, 616 69, Brno, Czech Republic

^b Hanon Systems Autopal s.r.o, Závodní 1007, 687 25, Hluk, Czech Republic

ARTICLE INFO

Keywords:

Plastic heat exchanger
Staggered tube bank
Air cross-flow
Heat transfer coefficient
Pressure drop
Microtube radiator

ABSTRACT

The thermal performance of low-temperature radiators constructed from staggered banks of stainless steel microtubes (SST unit) and polymeric fibers (PF unit, polyamide 612) was investigated in air cross-flow conditions. Tests were performed in a calorimetric wind tunnel according to automotive standards with air velocities of 2–10 m/s and coolant flow rates of 6–60 l/min. Experimental results demonstrated that airside pressure drops for SST and PF radiators are nearly identical, with a difference of approximately 1 %, showing that tube material did not influence airside pressure drops. Regardless of the 50-time difference in thermal conductivity between stainless steel (12 W/(m·K)) and polyamide (0.24 W/(m·K)), the heat transfer rate of the PF radiator was, on average, only 7 % lower than ST, with smaller deviations observed at lower air velocities. The Gaddis and Gnielinski model showed good prediction, with average discrepancies of 3 % for heat transfer rate, 7 % for overall and airside heat transfer coefficients, and 5 % for pressure drops. The results confirm that, when middle buffers are used, polymeric hollow-fiber radiators can be a viable lightweight alternative to metals for low-to-moderate airflow applications (2–10 m/s air speed).

1. Introduction

The exploration of microchannel heat exchangers represents a paradigm shift in thermal management, driven by the increasing demand for efficient heat dissipation from compact devices [1]. Microchannel heat exchangers, characterized by their high primary surface area-to-volume ratio (approx. 290 m²/m³ for units tested in this study), offer enhanced heat transfer capabilities compared to traditional heat exchangers, making them suitable for applications ranging from microelectronics cooling to automotive air conditioning and aerospace systems [2–4].

In automotive thermal management, microchannel radiators and condensers have become common – these typically involve flat multi-port microtubes with air flowing across them. While not circular tubes, they operate on the same principle of many small channels increasing surface area. Empirical studies on automotive microchannel heat exchangers (e.g., A/C condensers) found significantly improved heat transfer per volume compared to traditional round-tube heat exchangers [5]. Likewise, Mezzo in motorsports introduced microtube radiators for race cars, featuring on the order of 10 000 stainless steel tubes of ~0.5 mm diameter in a core [6]. Wind tunnel tests of these racing radiators demonstrated excellent thermal performance with relatively low air-side

* Corresponding author.

E-mail address: ilya.astrouski@vut.cz (I. Astrouski).

<https://doi.org/10.1016/j.csite.2026.107681>

Received 22 October 2025; Received in revised form 26 December 2025; Accepted 8 January 2026

Available online 14 January 2026

2214-157X/© 2026 The Authors. Published by Elsevier Ltd. This is an open access article under the CC BY license (<http://creativecommons.org/licenses/by/4.0/>).

pressure drops. Owing to the elimination of louvered fins (air flows directly around tubes, reducing flow resistance and fouling). Success in racing (IndyCar) and subsequent adoption in some aerospace systems (for example, drone or satellite thermal control) show that microtube banks can offer high-performance cooling with weight and volume savings [6].

In microtube arrays, air flow can range from laminar to turbulent, and heat transfer and pressure drop are strongly dependent on the tube pattern and flow conditions. This study is intended to address the comparison of two tube materials, stainless steel and polyamide. Stainless steel and polymeric material can be considered competitors, taking into account the high chemical stability and resistance to corrosion of both materials. It will allow the application of these materials in conditions where an aggressive acidic atmosphere can be present [7].

Although good correlation with analytical equations was found for stainless steel tubes, the plastic material itself can cause a significant shift in behavior, as shown by Kroulikova [8].

In designing tube bank heat exchangers, engineers often rely on empirical Nu–Re correlations and friction factor formulas derived for macroscale tube bundles. These classical correlations are typically based on experiments for tube diameters of order centimeters and larger, in turbulent flow regimes. They provide Nusselt number as a function of Reynolds (and Prandtl number) with different coefficients for in-line vs. staggered arrangements (see Fig. 1) and correction factors for the number of tube rows. The layout of microtubes (where S_T is the transverse pitch and S_L is the longitudinal pitch, respectively) has a first-order impact on heat transfer and pressure drop. In an in-line array, tubes in successive rows align with those upstream, creating clear flow channels between columns of tubes. In a staggered array, each tube is offset from the one in front of it (often arranged on a triangular lattice) so that the flow is continually disrupted. Staggered configurations generally yield higher heat transfer because each tube is more exposed to the flow and the wake of upstream tubes impinges on downstream tubes, enhancing mixing. However, the applicability of the equations derived from experimental data achieved on macro-scale tubes is questionable for microtube banks. A recent review noted that the correlations for round tube banks have only been validated at conventional scales [9], and others proposed correction factors to account for small tube effects [10].

Thus, we decided to evaluate the standardly used correlation (VDI Heat Atlas, Gaddis and Gnielinski model [11]) for staggered-arranged tube banks made of both stainless steel and polymeric materials.

2. Theoretical considerations

This chapter aims to describe the theory and equations allowing to calculate air pressure drops and heat transfer on bank of microtubes. The presented models and equations will be compared with experimental results afterwards.

2.1. Pressure drop of tube bundle in air cross-flow

The correlations used are described in detail in section L1.4 of VDI Heat Atlas [11]. The equations are valid for both inline and staggered tube arrangements in a wide range of Reynolds numbers Re and cover laminar ($Re < 100$), transition ($100 < Re < 10^4$), and turbulent regimes ($10^4 < Re < 2 \times 10^5$). The equations are the result of the superposition of equations of Bergelin et al. for laminar flow in a modified form [12] and the equations of Gaddis and Gnielinski [13] for turbulent flow.

The pressure drop Δp , across the tube bundle due to friction and flow separation in the wake region behind the individual tubes may be calculated from

$$\Delta p = \xi n_{MR} \frac{\rho w_e^2}{2} \quad \text{Eq. 1}$$

In Eq. (1), ξ is the drag coefficient, n_{MR} is the number of main resistances in the flow direction, ρ is the density, and w_e is the mean flow velocity in the narrowest cross section. For a staggered tube arrangement with the narrowest cross-section between adjacent tubes in the same row, the number of main resistances in the flow direction n_{MR} is identical to the number of tube rows.

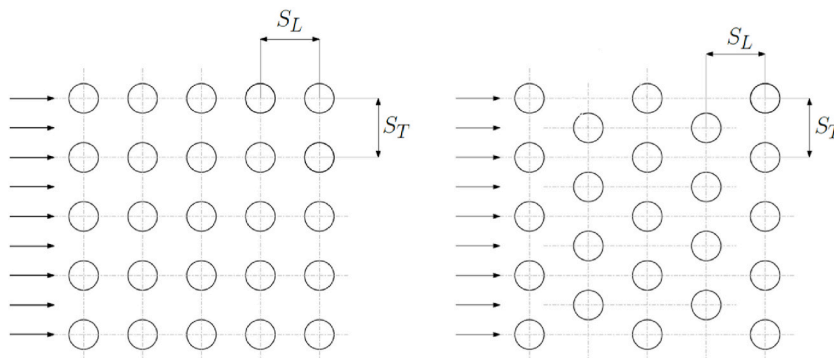


Fig. 1. Inline (left) and staggered arrangement scheme.

The drag coefficient ξ is a function of the Re , the transverse pitch ratio a , and the longitudinal pitch ratio b , where

$$Re = \frac{w_e D_o \rho}{\eta} \quad \text{Eq. 2}$$

$$a = \frac{S_T}{D_o}, b = \frac{S_L}{D_o}, w_e = \frac{a}{a-1} w_f \quad \text{Eq. 3}$$

It needs to be noted that w_e is the air velocity in the narrowest cross-section, while w_f is the velocity of free flow incoming to the tube bundle.

The drag coefficient for an ideal tube bundle with staggered tube arrangement may be calculated from the following equations

$$\xi = \xi_{lam} + \xi_{turb} F_v \quad \text{Eq. 4}$$

with

$$F_v = 1 - \exp\left(-\frac{Re + 200}{1000}\right) \quad \text{Eq. 5}$$

The drag coefficient ξ_{lam} for laminar flow is given by

$$\xi_{lam} = \frac{f_{a,Lv}}{Re} \quad \text{Eq. 6}$$

with

$$f_{a,Lv} = \frac{280\pi \left[(b^{0.5} - 0.6)^2 + 0.75 \right]}{(4ab - \pi) a^{1.6}}, \text{ for } b \geq 0.5\sqrt{2a+1} \quad \text{Eq. 7}$$

The drag coefficient ξ_{turb} for turbulent flow is given by

$$\xi_{turb} = \frac{f_{a,t,v}}{Re^{0.25}} \quad \text{Eq. 8}$$

with

$$f_{a,t,v} = 2.5 + \left(\frac{1.2}{(a - 0.85)^{1.08}} \right) + 0.4 \left(\frac{b}{a} - 1 \right)^3 - 0.01 \left(\frac{a}{b} - 1 \right)^3 \quad \text{Eq. 9}$$

2.2. Determination of the heat transfer coefficient in a tube bundle

The average Nusselt number in a cross-flow over a bundle of smooth tubes can be calculated from that in a cross-flow over a single tube [(VDI Heat Atlas [11], section G7.3)]. However, if the flow velocity is the same in both cases, the Nusselt number for a tube in a bundle is higher than that for a single tube exposed to this velocity in free flow. The enhancement depends on the longitudinal pitch and the transverse pitch of the bundle.

$$(h_o \cdot D_o) / k_{air} = Nu_{o,bundle} = f_A Nu_{l,0} \quad \text{Eq. 10}$$

There is no need to use a correction factor accounting with the number of rows (if row number is higher than 10) and the correction factor for temperature dependence of physical properties (as considered approximately 1 for air [see chapter G8.4.3 of Heat Atlas [11]). The void fraction and the arrangement factor f_A depend on the transverse pitch ratio a and the longitudinal pitch ratio b (see Eq. (3)) in the tube bundle and are given by

$$\psi = 1 - \frac{\pi}{4a}, \text{ for } b \geq 1 \quad \text{Eq. 11}$$

$Nu_{l,0}$ can be calculated as

$$Nu_{l,0} = 0.3 + \sqrt{Nu_{l,lam}^2 + Nu_{l,turb}^2} \quad \text{Eq. 12}$$

where

$$Nu_{l,lam} = 0.664 \sqrt{Re_{\psi,l}} \sqrt[3]{Pr} \quad \text{Eq. 13}$$

$$Nu_{l,turb} = \frac{0.037 Re_{\psi,l}^{0.8} Pr}{1 + 2.443 Re_{\psi,l}^{-0.1} (Pr^{2/3} - 1)} \quad \text{Eq. 14}$$

and

$$Re_{\psi,l} = \frac{w_f l}{\psi L} \quad 10 < Re_{\psi,l} < 10^6, l = (\pi/2)D_o \quad \text{Eq. 15}$$

The factor for the staggered tube arrangement is

$$f_{A,stag} = 1 + \frac{2}{3b} \quad \text{Eq. 16}$$

2.3. Determination of the heat transfer coefficient in microtubes

For fully developed laminar flow (Influence of the undeveloped flow region in negligible), the limiting inside Nusselt number can be found [14] as:

$$Nu_{T3} = \frac{\frac{48}{11} + Nu_w}{1 + \frac{59}{220} Nu_w} \quad \text{Eq. 17}$$

$$Nu_w = \frac{U_w D_i}{k_{cool}} \quad \text{Eq. 18}$$

$$\frac{1}{U_w} = \frac{D_i}{D_o h_o} + \frac{D_i}{2k_w} \quad \text{Eq. 19}$$

where k_{cool} is the thermal conductivity of the coolant inside the fibers (microtubes), and k_w is the thermal conductivity of the plastic/metal tube wall and h_o is coefficient of heat transfer on outer surface of the tube calculated as in chapter above.

2.4. Determination of the overall heat transfer coefficient and the heat transfer rate

The overall heat transfer coefficient (based on outer tube surface) was calculated as:

$$U = \frac{1}{\left(\frac{1}{D_o \cdot h_o} + \frac{\ln(D_o/D_i)}{2k_w} + \frac{1}{D_i \cdot h_i} \right) D_o} \quad \text{Eq. 20}$$

To obtain a heat transfer rate, the Effectiveness-NTU method was used (as in Incropera & DeWitt, 1996 [15]). The number of transfer units (NTU) was obtained by the following relationships:

$$NTU = \frac{U \cdot A}{C_{min}}, \quad \text{Eq. 21}$$

where C_{min} is the minimum of heat capacity rates on coolant and air, where A is the heat transfer area of the outside surface.

Because the tube liquid flows through a large number of small-diameter fibers, we considered the tube liquid (coolant) unmixed. On the other hand, the air flowing around the tube bank should be considered as mixed. If the outside flow heat capacity rate value C_o was higher than the inside one C_i then effectiveness is calculated as:

$$\varepsilon = \left(\frac{1}{C_r} \right) (1 - \exp\{-C_r[1 - \exp(-NTU)]\}) \quad \text{Eq. 22}$$

For a higher inner flow heat capacity rate, the effectiveness was calculated as:

$$\varepsilon = 1 - \exp(-C_r^{-1}\{1 - \exp[-C_r(NTU)]\}) \quad \text{Eq. 22}$$

The maximum possible and actual heat transfer rate were obtained by

$$Q_{max} = C_{min} \cdot (T_{cool1} - T_{a1}) \quad \text{Eq. 24}$$

$$Q = \varepsilon \cdot Q_{max} \quad \text{Eq. 25}$$

3. Experimental details

3.1. Parameters of the tested heat exchangers

Table 1 contains all the parameters, and Figs. 2 and 3 present the photos of the tested units, STT (stainless steel tubes), and PF (polymeric fibers made of polyamide 612). It was decided to test two prototypes in order to compare these two materials. Parameters characterizing the structure are the transversal pitch S_T and the longitudinal pitch S_L , as illustrated in Fig. 1.

CNC drilling was used to drill the holes for tubes/fibers in each of the tube plates made of fiberglass-enforced epoxy resin. Each fiber was then inserted through all separating baffles (placed every 5 mm) and manifold plates. The manifold plates were connected with 3D

printed manifold chambers (printed of PA 3200 GF, glass-filled polyamide 12 material) to create a uniform coolant supply to all the tubes. The internal geometry of the manifolds follows the optimized geometry of functional automotive radiators.

3.2. Test equipment, procedure, and error analysis

Standard procedure of testing according to the automotive standard is to test $m \times n$ points with a combination of m values of air velocity and n values of coolant flow rate. In this measurement, three values of air velocities and three values of coolant flow rates were used, which resulted in 9 measured points for both units, 18 test points total. The described set of measurement points covers a wide range of regimes and cooling intensities and serves as comprehensive information about heat exchanger performance and efficiency. Every measurement point is obtained from a 5-min recording after reaching steady state conditions, with final values being time averages from this period. Each recording is preceded by a necessary air removal and stabilization of the reported values to reach a steady state. Industry-certified calorimetric circuit RAIIV (wind tunnel), having a measurement accuracy of 5 % according to automotive standards, was used for the testing. It consists of two circulation cycles connected to the heat exchanger (see Fig. 4) (see Fig. 5).

The calorimeter is equipped to measure automotive radiators' heat performance and pressure drop. For this reason, a mixture of 50 % water and 50 % ethylene glycol (coolant) is used as the medium in the tested units. The temperatures of the coolant upstream and downstream, the flow rate, and the pressure drop are measured. The airside temperature is measured upstream and downstream of the heat exchanger, and the airflow rate and pressure drop are monitored. The air is preheated to the initial temperature by an electric heater. The inlet and outlet temperatures of both air and the coolant, as well as the pressure drops and flow rates, are monitored at a frequency of 1 Hz. The mass flow rates of both media and the heat transfer rate are then calculated by the software included in the calorimeter based on the volumetric flow rates. The equipment is set up and calibrated to provide 3 % precision of heat transfer rate measured on coolant side for air velocity 2 m/s and higher. To ensure proper equipment calibration and test result repeatability, the calibrated radiator master sample is tested every quarter and test equipment is recalibrated if necessary. The calorimeter parameters set for the experiment are in Table 2.

3.3. Data reduction

This chapter is intended to describe briefly how experimentally obtained data (air and glycol flow rates, temperatures, heat transfer rates) were used to derive the overall and local convective heat transfer coefficients which are to be compared with the ones calculated (as in section Theoretical consideration).

Both tested heat exchangers were tested in a cross-flow regime. To derive the overall heat transfer coefficient, the LMTD method with a cross-flow correction factor is used. The overall heat transfer coefficient was calculated as:

$$U = \frac{Q}{A F \Delta T_{lm}} \quad \text{Eq. 26}$$

where Q is the rate of heat transfer, U is the overall heat transfer based on the outer surface heat transfer area A , the ΔT_{lm} is the logarithmic mean temperature difference, and F is the correction factor for LMTD calculated according to Jeter [16]. Thermal properties of 50 % ethylene glycol and air were estimated as those defined for the average fluid temperature of the inlet and outlet. As the outer convective coefficient and wall thermal resistance influence the inner boundary conditions (of laminar flow), Eq. (20) is solved in combination with Eq. (17)–(19) (inverse task), and the solution requires solving a quadratic equation with one root leading to both convective coefficients. The process is described in detail in by Song [14].

Table 1
Parameters of tested heat exchangers.

Sample	SST	PF
Tube material	Stainless steel	polyamide 612
tube o.d./i.d., mm	1.2/1	1.23/0.99
tube wall thickness, mm	0.1	0.12
Tube wall conductivity, W/(m·K)	12	0.24
Number of tube rows	12	12
no. of tubes	1134	1134
effective tube length, mm	360	360
total tube length, mm	400	400
Tube spacing S_r , mm	4.97	4.97
Row spacing S_l , mm	2.62	2.62
Supporting baffle spacing, mm	5	5
Heat transfer area (OD), m ²	1.54	1.58
Surface area to volume ratio, m ² /m ³	284	292
Overall dimensions, mm	490x420x32	490x420x32
flow mode		Cross-flow
Max. test pressure		4 bar
Max. test temperature		120 °C

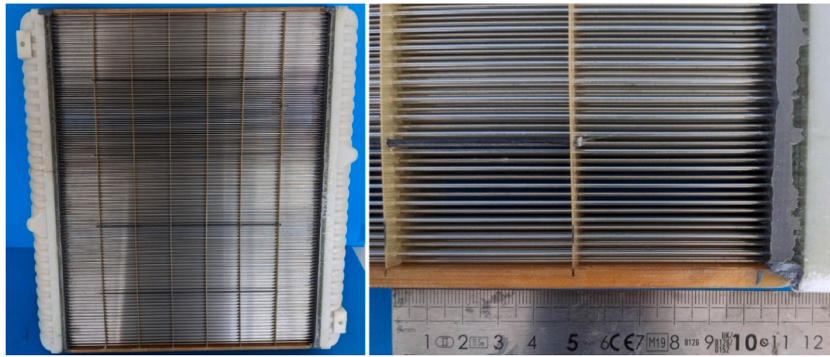


Fig. 2. SST: steel tubes, staggered arrangement, cross-section 470x360 mm.

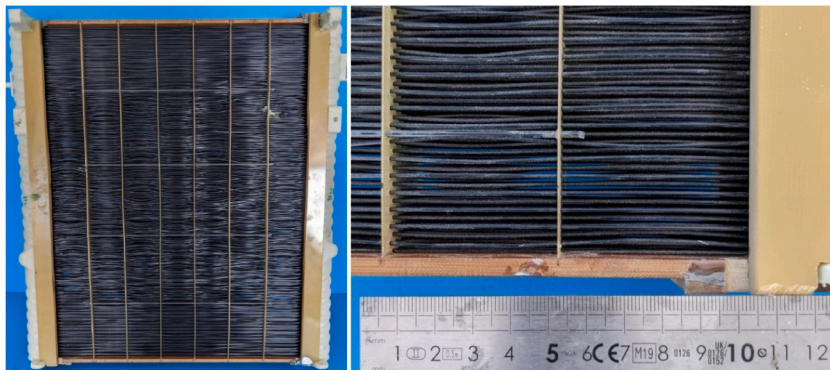


Fig. 3. PF: Polyamide 612 fibers, staggered arrangement, cross-section 470x360 mm.

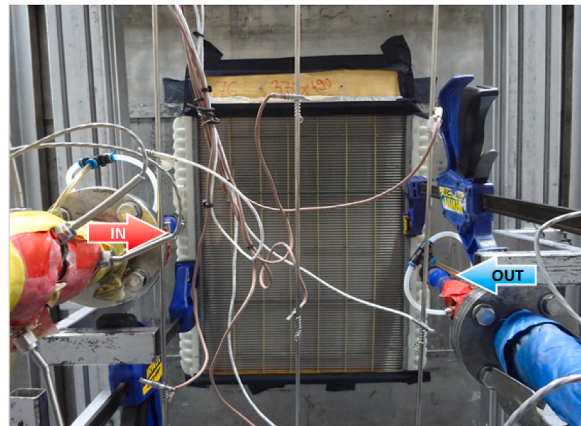


Fig. 4. – Unit SST during the testing – a frontal view.

3.4. Uncertainty analysis

The testing equipment used for data acquisition measured the inlet/outlet temperature and flow rates of liquids on both sides. The thermal outputs measured on the air side were used to calculate the thermal performance, as the values of the heat transfer rate on the coolant side were slightly higher (2.8 % in a average) and influenced by radiators headers and connections. The equipment is set up and calibrated to provide a 3 % precision of the heat transfer rate measured on the coolant side for air velocities of 2 m/s and higher. To ensure proper equipment calibration and test result repeatability, the calibrated radiator master sample is tested every quarter, and the test equipment is recalibrated if necessary.

The thermal balance error of 18 experiments had a mean thermal balance error of 2.8 %. The highest thermal balance errors

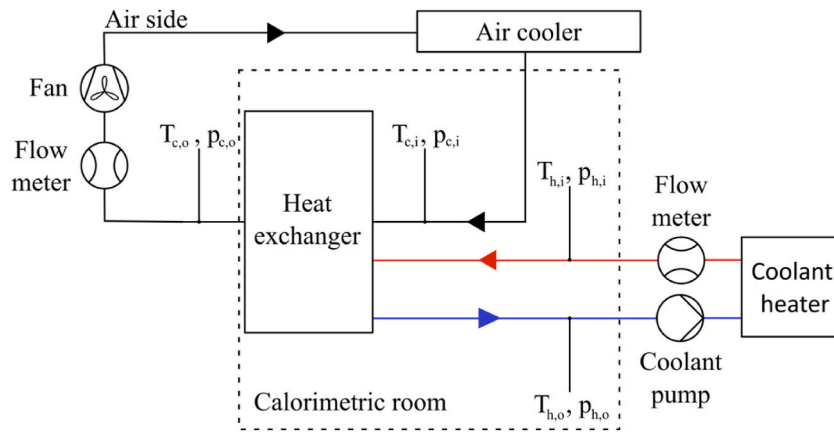


Fig. 5. – Experimental setup scheme: calorimetric room, wind tunnel and coolant circuit.

Table 2

Standard deviations used in uncertainty analysis.

Parameter	Parameter details	Standard deviation
Dimensional parameters	Number of tubes, tube outer/inner diameter, tube length	2 % of the measured value
Tube material thermal conductivity	Thermal conductivity of polyamide 612 (0.24 W/mK) and stainless steel (12 W/mK)	5 % of the measured value
Air speed, coolant flow rate	Airflow measured by calibrated mass flow rate inserts	3 % of the measured value
Temperatures	All temperatures measured by PT100 class A sensors	0.15 K

(average 6.1 %, maximum of 9.7 %) were found for experiments with 2 m/s airflow, while the experiments with 6 and 10 m/s airflow had a thermal balance average error of only 0.9 %.

To estimate the uncertainty of the calculated values of the overall heat transfer coefficient and air convective heat transfer coefficient, the Monte Carlo method was used. Using the Monte Carlo is very suitable for cases like this as it can show variation of the derived values depending on the random variation of the input data within the defined error range. For the heat transfer rate, the standard deviation was considered to be 3 % (as guaranteed by testing precision). The standard deviations of other parameters were set as in Table 2.

A simulation of 500 random input values was performed separately for the SST and PF units, under conditions of minimal and maximal flow rates of coolant and air. The pressure drops were measured using differential pressure manometers with a precision of ± 5 % directly, so these values are presented as uncertainty values. All the uncertainty values are presented in Table 3.

4. Results and discussion

Table 3 provides the compilation of experimental results (9 test points) for both SST and PF units. There is a similarity in the test results for units SST and PF – thermal performance, pressure drop of coolant, and air. These results will be discussed in more detail and compared with theoretical predictions. *Re* values (approx. 210–1120) show that all the test points are in transient flow regime.

Fig. 6 presents the dependence of air pressure drop on velocity for both SST and PF units (experimental data), combined with the modelled results by the Gaddis and Gnielinski model. As expected, the pressure drop rises with increasing velocity, following a trend of pressure drop quadratic growth vs air velocity.

The experimental measurements for both SST and PF lay very close to each other, showing marginal to no influence of tube material on air pressure drops (difference of less than 1 %). It is important to note that such behavior is found due to the use of the intermediate baffles supporting the plastic tubing to be fixed in a prescribed position. Previous studies [8] showed that the polymeric tubing can vary its behavior significantly (move and change bank pattern) if exposed to heat due to a decrease in stiffness in high-velocity airflow.

Test results (for both SST and PF) are in good correlation with the model predictions. When for low air speed 2 m/s the prediction vs test is not sufficient (–46 % discrepancy in average), for higher speed (6–10 m/s) the prediction's precision lies in the range of –12 to

Table 3

Uncertainty of the results represented by standard deviation.

	Test condition	U_o , %	h_o , %	dP_{air} , %
SST	(2.1 m/s air, 6 l/min coolant)	2,5	3,1	5
	(10.7 m/s air, 30 l/min coolant)	3,4	5	
PF	(2 m/s air, 6 l/min coolant)	2,7	4	5,8
	(10.7 m/s air, 30 l/min coolant)	3,5	5,8	

+5 %, with average discrepancy of -3 %, confirming the reliability of the model. Not sufficient correlation for 2 m/s velocity can be explained by low values of pressure drops to be measured (15 Pa is the theoretically predicted value vs 27 Pa of the test) and can be associated with both the pressure transducer's precision and extra pressure drop occurring around the tested sample, not in the tested sample core.

Fig. 7 shows the experimental data and the theoretical prediction of the heat transfer rate vs air velocity. Firstly, it is important to notice the relatively low difference in thermal performance between the SST sample and the PF sample. Regardless of the 50 times difference in thermal conductivity (stainless steel tubes with $12 \text{ W}/(\text{m}^2\text{K})$ conductivity vs polyamide tubes with $0.24 \text{ W}/(\text{m}^2\text{K})$), the average decrease in predicted heat transfer is only 7 % on average. The performance difference of tube material stainless steel vs polyamide is least pronounced for 2 m/s air flow (-5 % calculated, -5.8 % in test), bit more pronounced for 6 m/s (-10.1 % calculated, -2.2 % in test) and the most pronounced for 10 m/s (-12.6 % calculated, -6.3 % in test) when the air side heat transfer is the highest. The correlation between the predictive model of Gaddis and Gnielinski and experimental data is very good, with an average discrepancy of only 3.2 % (8 % maximum) for the SST unit and 2.5 % for the PF unit (8 % maximum).

Fig. 8 presents the variation of the overall heat transfer coefficient versus air velocity for both the SST and PF units. The average difference in overall heat transfer between PF and SST units (polymeric material vs stainless steel) is -13.7 %, with the smallest differences for 2 m/s airflow (-9.5 %) and the highest (-17.2 %) for 10 m/s airflow. It is evident that the influence of wall material depletes as the air speed decreases. Together with the previously mentioned fact that polymeric tubing resistance drops when heated, we can conclude that polymeric hollow fiber radiator systems are more favorable for applications with low-speed airflow (up to approximately 4 m/s). It is worth mentioning that the values of the heat transfer coefficient are high. For the SST unit, the range is from 182 (for 2 m/s) to $366 \text{ W}/(\text{m}^2\text{K})$ (for 10 m/s). For the PF unit, the range is from 165 (for 2 m/s) to $303 \text{ W}/(\text{m}^2\text{K})$ (for 10 m/s).

Considering the prediction with the Gaddis and Gnielinski model, the trend is similar to the results achieved for the heat transfer rate. Nevertheless, due to inverse dependence between the overall heat transfer coefficient and the heat transfer rate, the relative error is higher, 5 % for the PF unit, 7 % for the SST unit, and 6 % on average.

Fig. 9 illustrates the dependence of the air heat transfer coefficient (h_0 , $\text{W}/(\text{m}^2\text{K})$) on air velocity for SST and PF units, with experimental data compared against predictions by the Gaddis and Gnielinski model. The theoretical prediction curve is common for both units, as air-side heat transfer is independent of tube wall material. Model predictions follow a smooth nonlinear trend that captures the general rise of h_0 but tend to slightly underpredict at higher velocities compared with experimental points, especially for PF, where deviations can reach up to 15 %. Nevertheless, the average correlation of 9 % achieved for SST and 8 % for PF unit shows that the Gaddis and Gnielinski model is very suitable for predicting air-side heat transfer coefficient on the bank of microtubes. It is essential to keep in mind that the model correlations come from experimental results and are extrapolated to cover a wide range of air Reynolds numbers with a precision of approximately 10 %.

5. Conclusion

This work presented a comparison of low-temperature radiators built of staggered banks of stainless steel microtubes (SST) and polymeric fibers (PF) tested in air crossflow. Despite the significant difference in thermal conductivity between stainless steel ($12 \text{ W}/(\text{m}^2\text{K})$) and polyamide 612 ($0.24 \text{ W}/(\text{m}^2\text{K})$), the overall heat transfer coefficients of the PF unit were only 13.7 % lower. This indicates that conductivity has a secondary role when the dominant resistance lies on the air side, particularly under lower velocities (2–6 m/s air flow). Air-side pressure drops of both radiators were mostly identical, with less than 1 % difference for the tested velocity range, showing no influence of wall material.

The experimental data on pressure drops and heat transfer correlate well with the prediction by the Gaddis and Gnielinski model, which predicted heat transfer rates with a discrepancy of only 3.2 % and pressure drops within an accuracy of 5–10 %. Deviations at very low air velocities can be attributed to measurement sensitivity and secondary losses in the test setup.

Overall, the findings highlight that polymeric hollow fiber radiators can serve as competitive alternatives to stainless steel designs. They are a promising lightweight alternative for applications where reduced mass, corrosion resistance, and cost are essential, and airflow velocities remain reasonably moderate (up to 10 m/s). Replacing 1134 400-mm-long stainless steel microtubes with polyamide 612 fibers results in a decrease in tube material mass from 1.26 kg to 0.19 kg, representing a 1.07 kg (85 % of the tube mass) savings. The total mass of the full-plastic radiator (2.25 kg, including frame and headers) is 67 % of that of its metal-tube competitor (3.32 kg). Such a substantial weight saving presents a significant advantage for the thermal management systems of electric vehicles, which frequently operate under low airflow velocities due to idle conditions, urban driving, and auxiliary cooling of batteries and electronics. According to Del Pero [17], a 1 kg reduction in mass can lower energy use by ~ 0.005 – $0.01 \text{ kWh}/100 \text{ km}$ in an electric vehicle, thereby contributing to its efficiency.

While the operating costs of both types of tubes are similar (the same pumping costs, etc.), a change in material also enables a decrease in the cost of building the microtube radiator (CAPEX costs). As the total length of tubing is 454 m, a decrease in tube cost from 0.5 euro/m (precision-drawn steel tubing bought in large volumes) to 0.05 euro/m (100 m/min high-speed polymeric extrusion) results in a 90 % reduction in tubing cost, from 227 euro to 23 euro. It makes the microtube radiator design significantly more economically viable and ready for mass adoption compared to its current niche usage in racing cars, aerospace, and defense [6].

Weight savings, lower material costs, and inherent corrosion resistance of polymers compensate for the moderate reduction in heat transfer (~ 10 %). These advantages make polymeric microtube radiators particularly attractive for electric vehicles, drones, or satellites, where reduced mass is critical due to energy efficiency, payload capacity, and overall operational performance.

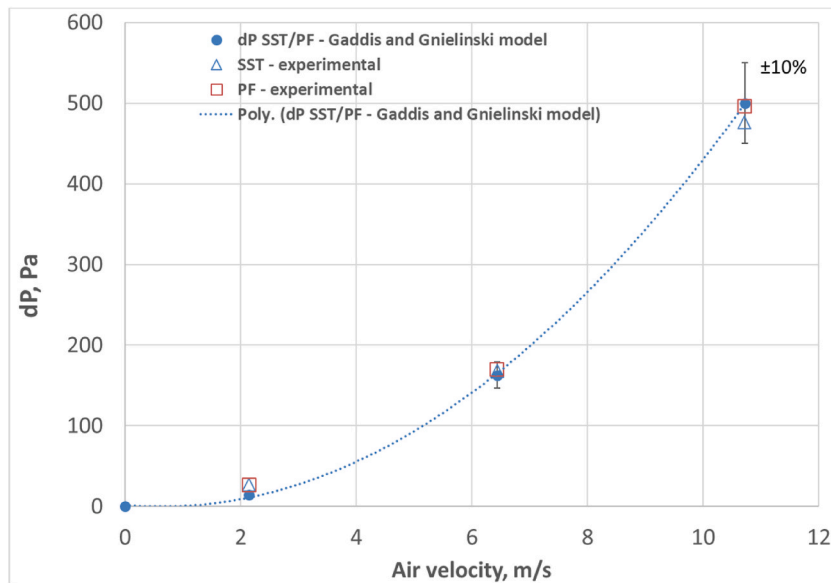


Fig. 6. – Air pressure drops vs air velocity.

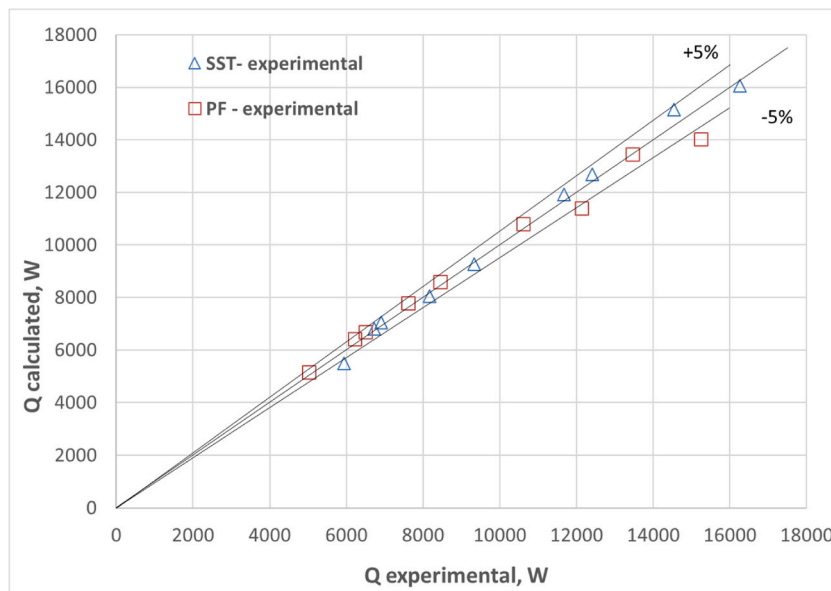


Fig. 7. – Heat transfer rate vs air velocity.

CRedit authorship contribution statement

Ilja Astrouski: Writing – original draft, Visualization, Validation, Supervision, Project administration, Formal analysis, Data curation, Conceptualization. **Krystof Mraz:** Writing – review & editing, Data curation. **Jan Bohacek:** Writing – review & editing, Supervision, Methodology, Conceptualization. **Ales Horak:** Writing – review & editing, Project administration, Methodology, Investigation, Data curation. **Erik Bartuli:** Writing – review & editing, Investigation.

Declaration of generative AI and AI-assisted technologies in the manuscript preparation process

During the preparation of this work, the author(s) used ChatGPT 5 and Grammarly in order to prepare the literature review, support writing, and grammar revision. After using this tool/service, the author(s) reviewed and edited the content as needed and take(s) full responsibility for the content of the published article.

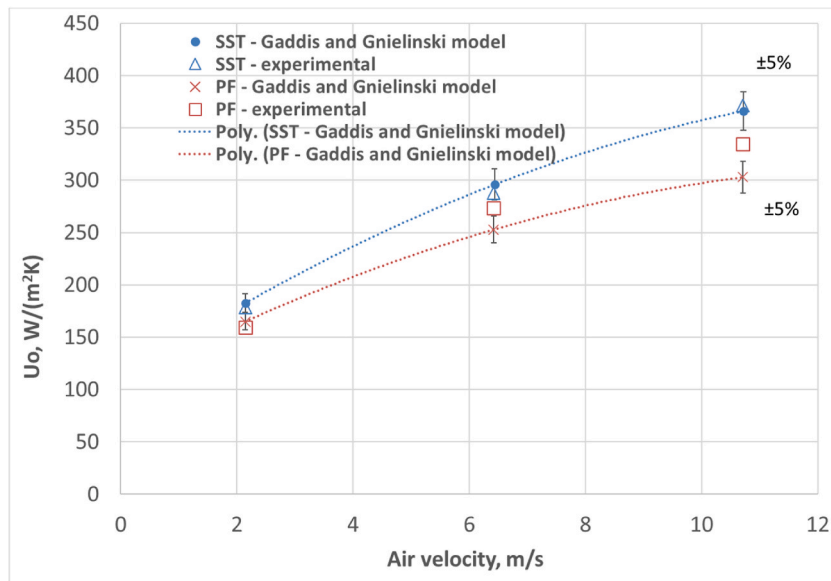


Fig. 8. – Overall heat transfer coefficient vs air velocity.

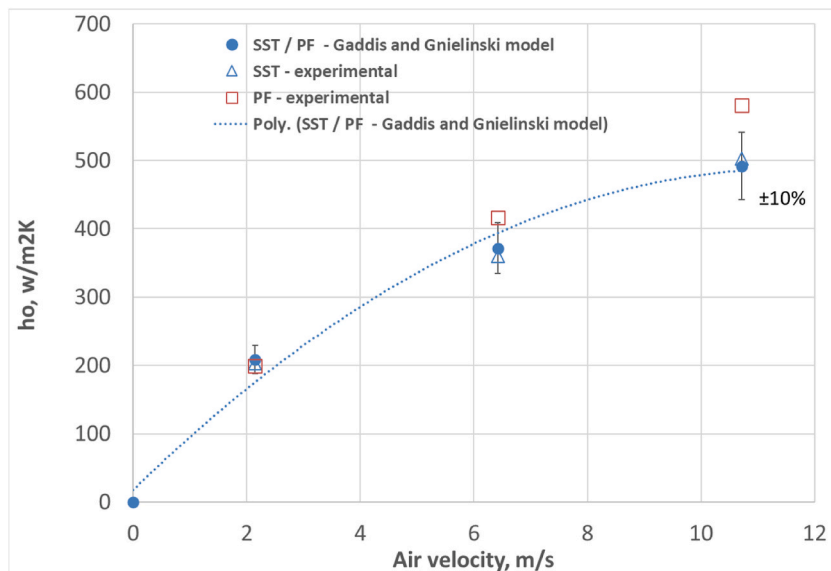


Fig. 9. – Air-side heat transfer coefficient vs air velocity.

Declaration of competing interest

The authors declare the following financial interests/personal relationships which may be considered as potential competing interests: Erik Bartuli reports financial support was provided by Ministry of Education, Youth and Sports. If there are other authors, they declare that they have no known competing financial interests or personal relationships that could have appeared to influence the work reported in this paper.

Acknowledgement

This work was supported by the project "Hollow Fiber Heat Exchangers with Reduced Permeability for Smart Cities", funded as project No. 8I24002 by Programme EIG CONCERT by the Ministry of Education, Youth and Sports of Czech Republic. <https://www.vut.cz/en/rad/projects/detail/35775>

Nomenclature

Symbol	Description
A	Outer heat transfer area [m ²]
a	the transverse pitch ratio, dimensionless
b	the longitudinal pitch ratio, dimensionless
C_{\min}	heat capacity rate, minimum of two streams, [W/K]
c_p	Specific heat capacity [J/(kg·K)]
C_r	Heat capacity rate ration, dimensionless
D_i, D_o	Inner, outer tube diameter, [m]
F	LMTD correction factor for cross-flow, dimensionless
$f_A, stag$	the tube arrangement factor (staggered), dimensionless
F_v	the drag coefficient factor, dimensionless
$f_{a,l}, f_{a,t,v}$	the drag coefficient factors, dimensionless
h_i	Inner (coolant side) heat transfer coefficient, [W/(m ² ·K)]
h_o	Outer (air side) heat transfer coefficient, [W/(m ² ·K)]
$k_{cool, air}$	Thermal conductivity of the coolant or air, [W/(m·K)]
k_w	Thermal conductivity of tube wall, [W/(m·K)]
L	half circumference of tube, [m]
n_{MR}	the number of main resistances to air flow (row number), dimensionless
NTU	Number of Transfer Units, dimensionless
$Nu_{0, bundle}$	mean Nusselt number for an ideal tube bundle, dimensionless
$Nu_{i,0}, Nu_{i,lam}, Nu_{i,turb}$	Nusselt number for a single tube in cross-flow, with laminar flow, with turbulent flow, dimensionless
Nu_{T3}	Nusselt number for developed laminar flow in circular tube with boundary conditions of the 3d type, dimensionless
Nu_w	Nusselt number corresponding to combined thermal resistance of outer convection (of air) and wall conduction, dimensionless
Δp	Air pressure drop across the tube bundle, [Pa]
Pr	Prandtl number, dimensionless
Q	Heat transfer rate, [W]
Q_{\max}	Heat transfer rate (maximal), [W]
Re	Reynolds number (acc. to Eq. (2)), dimensionless
$Re_{\psi,l}$	Reynolds number for a tube bundle (acc. to Eq. (15)), dimensionless
S_L	longitudinal pitch of tubes, [m]
S_T	transverse pitch of tubes, [m]
ΔT_{lm}	Logarithmic mean temperature difference, [K]
T_{cool}, T_{a1}	Inlet temperature of coolant, air, [K]
U	overall heat transfer coefficient, [W/(m ² ·K)]
U_w	heat transfer coefficient corresponding to combined thermal resistance of outer convection (of air) and wall conduction, [W/(m ² ·K)]
w_e	air velocity in the narrowest cross-section, [m/s]
w_f	free-stream air velocity upstream, [m/s]
PF	Polymeric Fiber unit (Polyamide 612)
SST	Stainless Steel Tube unit
LMTD	Logarithmic Mean Temperature Difference
VDI	Verein Deutscher Ingenieure (German Engineering Association)
RAIV	Automotive calorimetric wind tunnel used for experiments

Greek Letters, Subscripts and Superscripts

Symbol	Description
ϵ	Heat exchanger effectiveness, dimensionless
η	Dynamic viscosity, [kg/(m·s)]
ν	Kinematic viscosity, [m ² /s]
ξ_{lam}, ξ_{turb}	Drag coefficient laminar, turbulent, dimensionless
ρ	Air density [kg/m ³]
ψ	Void fraction, dimensionless

Data availability

Data will be made available on request.

References

- [1] L.S. Maganti, P. Dhar, T. Sundararajan, S.K. Das, Heat spreader with parallel microchannel configurations employing nanofluids for near-active cooling of MEMS, *Int. J. Heat Mass Tran.* 104 (2017) 1163–1175.
- [2] H. Li, Y. Li, B. Huang, T. Xu, Numerical investigation on the optimum thermal design of the shape and geometric parameters of microchannel heat exchangers with cavities, *Appl. Therm. Eng.* 171 (2020) 114965.

- [3] T. Kudelova, T. Kroulikova, I. Astrouski, M. Raudensky, The influence of the fibres arrangement on heat transfer and pressure drop of polymeric hollow fibre heat exchangers, *Appl. Therm. Eng.* 140 (2018) 72–81.
- [4] J. Hejck, P. Charvat, L. Klimes, I. Astrouski, A PCM-water heat exchanger with polymeric hollow fibres for latent heat thermal energy storage: a parametric study of discharging stage, *Energy Convers. Manag.* 198 (2019) 111893.
- [5] N. Saleem, C.C. Wang, K.H. Chen, Airside thermal performance of louvered fin flat-tube heat exchangers with different redirection louvers, *Appl. Therm. Eng.* 130 (2018) 725–737.
- [6] Mezzo Technologies, Microtube radiators for motorsports and aerospace, Available online: <https://mezzotechnologies.com/>. (Accessed 3 August 2025).
- [7] M. Raudensky, I. Astrouski, T. Brozova, Cooling of flue gas by cascade of polymeric hollow fiber heat exchangers, *Appl. Therm. Eng.* 127 (2017) 792–801.
- [8] T. Kroulikova, I. Astrouski, T. Kudelova, M. Raudensky, Crossflow polymeric hollow fiber heat exchanger: fiber tension effects on heat transfer and airside pressure drop, *Appl. Therm. Eng.* 123 (2017) 711–720.
- [9] A. Qasem, Compact and microchannel heat exchangers: a comprehensive review of airside friction factor and heat transfer correlations, *Renew. Sustain. Energy Rev.* 91 (2018) 1–15.
- [10] H. Li, Y. Li, B. Huang, T. Xu, Simulation study on flow and heat transfer of cross-arrangement tube bundle, *Int. J. Therm. Sci.* 134 (2018) 54–62.
- [11] VDI Heat Atlas, second ed., Springer, Berlin, 2010.
- [12] O.P. Bergelin, A.P. Colburn, H.L. Hull, Heat transfer and pressure drop during viscous flow across un baffled tube banks. University of Delaware, Engineering Experimental Station Bulletin No. 2 (1950). Newark, DE.
- [13] E.S. Gaddis, V. Gnielinski, Druckverlust in querdurchströmten Rohrbündeln, *Verfahrenstechnik* 17 (1983) 410–418.
- [14] L. Song, B. Li, D. Zarkadas, K.K. Sirkar, Polymeric hollow-fiber heat exchangers for thermal desalination processes, *Ind. Eng. Chem. Res.* 49 (2010) 11961–11977.
- [15] F.P. Incropera, D.P. DeWitt, *Fundamentals of Heat and Mass Transfer*, fourth ed., Wiley, New York, 1996.
- [16] S.M. Jeter, Effectiveness and LMTD correction factor of the cross-flow exchanger: a simplified and unified treatment, in: ASEE Southeast Section Conference, 2006.
- [17] F. Del Pero, L. Berzi, A. Antonacci, M. Delogu, Automotive lightweight design: simulation modeling of mass-related consumption for electric vehicles, *Appl. Sci.* 11 (3) (2021) 51.